Detecting shocked intergalactic gas with X-ray and radio observations

F. Vazza[1,2,3], S. Ettori[4,5], M. Roncarelli[1,4], M. Angelinelli[1], M. Brüggen[2], and C. Gheller[6]

[1] Dipartimento di Fisica e Astronomia, Universitá di Bologna, Via Gobetti 93/2, 40122 Bologna, Italy
e-mail: `franco.vazza@hs.uni-hamburg.de`
[2] Hamburger Sternwarte, Gojenbergsweg 112, 21029 Hamburg, Germany
[3] Istituto di Radioastronomia, INAF, Via Gobetti 101, 40122 Bologna, Italy
[4] INAF, Osservatorio di Astrofisica e Scienza dello Spazio, Via Pietro Gobetti 93/3, 40129 Bologna, Italy
[5] INFN, Sezione di Bologna, Viale Berti Pichat 6/2, 40127 Bologna, Italy
[6] Swiss Plasma Center, EPFL, SB SPC Station 13, 1015 Lausanne, Switzerland

ABSTRACT

Detecting the thermal and non-thermal emission from the shocked cosmic gas surrounding large-scale structures represents a challenge for observations, as well as a unique window into the physics of the warm-hot intergalactic medium. In this work, we present synthetic radio and X-ray surveys of large cosmological simulations in order to assess the chances of jointly detecting the cosmic web in both frequency ranges. We then propose best observing strategies tailored for existing (LOFAR, MWA, and XMM) or future instruments (SKA-LOW and SKA-MID, *Athena*, and eROSITA). We find that the most promising targets are the extreme peripheries of galaxy clusters in an early merging stage, where the merger causes the fast compression of warm-hot gas onto the virial region. By taking advantage of a detection in the radio band, future deep X-ray observations will probe this gas in emission, and help us to study plasma conditions in the dynamic warm-hot intergalactic medium with unprecedented detail.

Key words. shock waves – X-rays: galaxies: clusters – large-scale structure of Universe – galaxies: clusters: intracluster medium – methods: numerical

1. Introduction

Numerical simulations (e.g. Cen & Ostriker 1999; Davé et al. 2001; Gheller et al. 2016; Martizzi et al. 2019) have shown that the most important mass component of the baryons in the cosmic web is the elusive warm-hot intergalatic medium (WHIM), a rarefied gas with densities $n \sim 10^{-5}-10^{-4}$ part cm^{-3} and temperatures $T \sim 10^5-10^7$ K. The WHIM most likely fills the volume within cosmic filaments as well as in the outskirts of galaxy clusters, and attains its temperature via strong ($\mathcal{M} \gg 10$) accretion shocks.

Detections of absorption lines through the WHIM of intracluster filaments have been claimed (e.g. Werner et al. 2008; Nicastro et al. 2010). More recently, Nicastro et al. (2018) reported the possible detection of two OVII absorbers in the X-ray spectrum of a quasar at $z \geq 0.4$, possibly tracing the WHIM.

In a few nearby galaxy clusters and limited to a few narrow sectors, the thermodynamical properties of the intracluster medium have been mapped with X-ray observations out to R_{100} (e.g. Simionescu et al. 2011; Urban et al. 2011). Others mapped the gas properties in concentric rings out to R_{200} by combining X-ray and Sunyaev–Zeldovich (SZ) data (Ghirardini et al. 2019; Ettori et al. 2019; Eckert et al. 2019). The ends of five massive filaments connected to the massive cluster A2744 have been observed with *XMM-Newton* (Eckert et al. 2015), possibly representing the first images of cosmic filaments in the X-ray band. This made it possible to estimate that $5-10\%$ of the mass fraction of missing baryons may be bound in such objects. Moreover, the study of the Sunyaev–Zeldovich effect from the outer region of clusters, either in single pointings of interacting clusters (Planck Collaboration VIII 2013; Bonjean et al. 2018) or in stacked observations of larger samples (Tanimura et al. 2019; de Graaff et al. 2019) has detected the hot ($\sim 10^7$ K) and very over-dense ($\sim 10-10^2 \rho/\langle\rho\rangle$) gas component, potentially contributing to $\sim 10-50\%$ of missing cosmic baryons.

Cosmological hydrodynamical simulations have shown that the WHIM follows the underlying galaxy distribution (see e.g. Nevalainen et al. 2015) and that its diffuse emission is responsible for a significant fraction of the unresolved X-ray background in very deep *Chandra* observations (see Roncarelli et al. 2006a; Hickox & Markevitch 2007), with a predicted surface brightness on the order of $1-5 \times 10^{13}$ erg/(cm^2 s deg^2) in the $\sim 0.5-1$ keV energy band, with uncertainties related to its metal composition (Ursino et al. 2010; Cen & Chisari 2011; Roncarelli et al. 2012). However, the systematic detection and characterization of single WHIM systems remain a challenge due to its low emissivity. Hence, efforts have focused on stacking and statistical studies on the (auto)correlation function of its X-ray signal (see e.g. Piro et al. 2009; Takei et al. 2011; Ursino et al. 2011; Cappelluti et al. 2012; Kolodzig et al. 2018).

The planned X-ray mission *Athena* X-ray observatory[1], expected to be launched by ~ 2030, holds great promise to detect the WHIM in absorption. Among its ambitious goals, *Athena* aims to trace the missing baryons in the intergalactic medium via detecting their absorption lines, through the emission of bright sources up to $z \sim 2$. It is expected that in total ~ 80 sources can be studied at the highest possible resolution for spectroscopic studies with the instrument X-IFO ($\Delta E = 2.5$ eV) (Barcons et al. 2012).

---

[1] `http://www.the-athena-x-ray-observatory.eu`

The limitation of this technique is that, of course, most of these sources are unpredictable and variable, and only a dozen bright enough sources per year may be detected to study filaments. Concepts for future high-resolution X-ray imagers, capable of further reducing the limiting effect of the X-ray background from unresolved point-like sources, have recently been presented in the context of the US Decadal Survey (e.g. Lynx The Lynx Team 2018, AXIS Mushotzky et al. 2019). In this work, we wish to explore a complementary approach, in which *Athena* detects the WHIM in emission.

Planelles et al. (2018) have recently presented detailed radiative transfer calculations of the X-ray emission from a cluster at $z \approx 0.3$, reporting that the emission from the WHIM only accounts for ∼5% in the [0.5–2] keV band and ∼1% in the [2–10] keV band. In general, the WHIM is found to have a more filamentary structure than the $\geq 10^7$ K gas phase, extending several Megaparsecs (Mpc) out from the virial regions of galaxy clusters. Using a larger volume with the Illustris-The Next Generation (TNG) suite, Martizzi et al. (2019) recently studied the WHIM properties from $z = 4$ to $z = 0$, confirming that most of the filaments are more baryon-rich than the cosmic average, but that they have a significantly lower metallicity than the Intra Cluster Medium (ICM), which makes their observability via X-ray observations challenging.

In addition to the X-ray window, also the radio window may be able to image the cosmic web, thanks to the current (e.g. the Low Frequency Array (LOFAR), the Murchison Widefield Array (MWA), the Australian Square Kilometre Array Pathfinder (ASKAP), MeerKAT) and future (e.g. the Square Kilometer Array, SKA) generations of large radio telescopes. Cosmological simulations have shown that filaments of the cosmic web are surrounded by strong and quasi-stationary accretion shocks (e.g. Ryu et al. 2003; Pfrommer et al. 2006; Vazza et al. 2011), at which a tiny fraction of relativistic electrons may be accelerated. This is similar to what occurs in radio relics or cluster radio shocks at the periphery of clusters (e.g. Hoeft & Brüggen 2007; Wittor et al. 2017; van Weeren et al. 2019).

A few radio observations have already claimed the detection of diffuse synchrotron emission from the shocked gas at the interface between galaxy clusters and filaments attached to them (Bagchi et al. 2002; Giovannini et al. 2010; Farnsworth et al. 2013; Vacca et al. 2018). Moreover, the observation of Faraday Rotation by filaments in the Coma cluster has been claimed (Bonafede et al. 2013). Recently, the signature in Faraday space of filaments overlapping with the emission of a $z = 0.34$ radio galaxy has been claimed by O'Sullivan et al. (2019). The detection of faint diffuse radio emission at the interface of pre-merger galaxy clusters has been reported using LOFAR-High Band Array (HBA) by Botteon et al. (2018) and Govoni et al. (2019).

Simulations have shown that the low surface brightness ($\leq \mu$Jy arcsec^{-2} at ∼100 MHz), highly polarized (∼70%), and large angular scale ($\geq 1°$) emission that is expected to be produced by the shocked cosmic web (e.g. Keshet et al. 2004; Brown 2011; Vazza et al. 2015b) makes the low-frequency radio spectrum ($\nu \leq 300$ MHz) the most suitable for a detection, owing to the typically superior sampling of short baselines in low-frequency radio telescopes. In particular, the radio continuum surveys of SKA-LOW should detect parts of the magnetic cosmic web, with statistics depending on the (unknown) details of particle acceleration and magnetic field distribution in such rarefied plasma (e.g. Vazza et al. 2015a,b, 2017a). Additional to this, also polarization surveys with the SKA-MID may be able to detect the Faraday Rotation signal from the terminal part of filaments connected to massive galaxy clusters, provided that a large statistics of polarized sources is available (Locatelli et al. 2018).

The exciting possibility of detecting both thermal and non-thermal emission from the cosmic web with joint X-ray and radio surveys is the subject of this work. In a pilot study for the "SKA-Athena Synergy White Paper" (Cassano et al. 2018, Sect. 5.2.1) we first investigated the potential for a synergy between SKA and *Athena* in the study of the rarefied cosmic web. Our first results suggest that cluster outskirts are promising targets, with a small but non-negligible fraction of the cosmic web that might be detectable by both instruments (working at their nominal maximum capabilities). This possibility will make it possible to study the WHIM with *Athena* not only via absorption lines towards high-z powerful sources, but also on a few, carefully selected objects. Based on these results, we use one of the largest cosmological magneto-hydrodynamical simulations ever produced to assess to what extent future X-ray and radio observations can constrain the physical properties of the WHIM.

The structure of the paper is as follows: in Sect. 2 we introduce our simulations, and in particular in Sect. 2.2 we introduce our methods to produce sky models of our simulated universes. In Sect. 3 we present our results for the intrinsic emission properties of the cosmic web in X-ray and radio bands, while in Sect. 3.3.3 we specifically investigate mock *Athena* and SKA observations of our fields, and in Sect. 3.3.4 we present preliminary simulations of future spectroscopic analyses with the X-ray Integral Field Unit (X-IFU). Physical and numerical limitations of our results are given in Sect. 4 before we conclude in Sect. 5.

2. Methods

2.1. Cosmological simulations

As in previous work (Vazza et al. 2017a, 2018a), we simulated a comoving 100^3 Mpc^3 box with a uniform grid of 2400^3 cells and 2400^3 dark matter particles, using the cosmological Magneto-Hydordinamical (MHD) code ENZO[2] (Bryan et al. 2014). The fixed (comoving) spatial resolution of this run is $\Delta x = 41.6$ kpc cell^{-1} while the fixed dark matter mass resolution is $m_{dm} = 8.62 \times 10^6 \, M_\odot$ per particle. We initialized magnetic fields at $z = 45$ as a simple uniform background of $B_0 = 0.1$nG (one order of magnitude below the upper limits on primordial magnetic fields from the analysis of the Cosmic Microwave Background (CMB), Planck Collaboration XIX 2015), and we used the MHD method of Dedner (Dedner et al. 2002), ported to Graphic Processing Units (Wang et al. 2010) to evolve magnetic fields at run-time.

Our run is non-radiative and does not include any treatment for star formation or feedback from active galactic nuclei. To a first approximation, these processes are not very relevant for the radio and X-ray properties of the peripheral regions of galaxy clusters and filaments, which are our main focus (see Sect. 4 for a discussion).

We assumed a ΛCDM cosmological model, with density parameters $\Omega_{BM} = 0.0455$, $\Omega_{DM} = 0.2265$ (BM and DM indicating the baryonic and the dark matter respectively), $\Omega_\Lambda = 0.728$, and a Hubble constant $H_0 = 70.2$ km/(s Mpc). In Sect. 3.3.4 we will also present results for the resimulation of a massive galaxy cluster with the same setup, but using nested initial conditions and adaptive mesh refinement (eight levels) to achieve a higher resolution ($\Delta x_8 \approx 4$ kpc cell^{-1}), similar to Vazza et al. (2018b). An impression of the three-dimensional distribution of magnetic

---

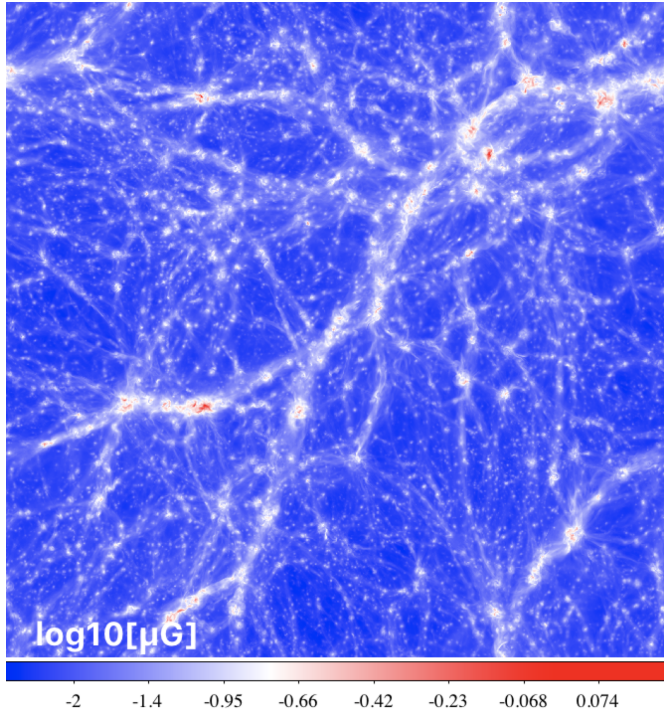[2] www.enzo-project.org

Fig. 1. Projected (mass weighted) magnetic field strength at $z = 0.05$ for our simulated $100^3 \, \mathrm{Mpc}^3$ volume.

fields in our simulation (which is one of the biggest MHD simulations ever performed in cosmology) is given in Fig. 1, and shows the variety of magnetic field strengths and configurations at $z = 0.05$.

2.2. Sky models

2.2.1. X-ray emission

For the X-ray emission, we assumed for simplicity a single temperature and a single (constant) composition for every cell in the simulation, and we computed the emissivity from the B-Astrophysical Plasma Emission Code (B-APEC)[3], assuming ionization equilibrium and including continuum and line emission. We consider a constant metallicity across the volume, $Z/Z_\odot = 0.3$ (see the discussion in Sect. 4 on the rather small impact of metallicity in most of our estimates). For each energy band, we computed the cell's X-ray emissivity, $S_X = n_H n_e \Lambda(T, Z) \mathrm{d}V$, where n_H and n_e are the number density of hydrogen and electrons (assuming a primordial composition) respectively, and $\mathrm{d}V$ is the constant volume of our cells.

We do not include the additional contribution from the inverse Compton emission from the same relativistic electrons accelerated by shocks and responsible for the radio emission (see next section), whose amplitude depends on the assumed electron energy distribution at low energies (e.g. Bartels et al. 2015). However, our estimates show that the inverse Compton in the [0.8–1.2] keV band is negligible ($\leq 1\%$) compared to the thermal emission of the cluster. It may start to dominate only at very large radii, $\geq 2-3 R_{100}$, at which no detection seems to be feasible with realistic exposure times.

The left panel of Fig. 2 shows the integrated X-ray emission from the simulated box located at $z = 0.05$, in the [0.8–1.2] keV

energy band. At the angular distance corresponding to this redshift ($D_A \approx 201.6 \, \mathrm{Mpc}$) this volume covers $28.4° \times 28.4°$. For reference, *Athena*'s Wide Field Imager field of view is $\sim 40' \times 40'$, while X-IFU's field of view is $\sim 5' \times 5'$.

2.2.2. Radio

We predict the synchrotron radio emission assuming that diffusive shock acceleration (DSA, e.g. Kang et al. 2012, and references therein) is able to accelerate a very small fraction of thermal electrons swept by shocks up to relativistic energies ($\gamma \geq 10^3 - 10^4$), and that the intergalactic medium has a non-negligible magnetic field, as suggested by our MHD simulation (e.g. Fig. 1). As in previous work (Vazza et al. 2015b), we identify shocks in the simulation in post-processing with a velocity-based approach, and we compute the radio emission from electrons accelerated in the shock downstream following Hoeft & Brüggen (2007). The typical efficiency (ξ_e) considered in the conversion efficiency from shock kinetic energy into the energy of relativistic electrons is small and it scales with the Mach number and the upstream gas temperature as in Hoeft & Brüggen (2007): for example it is $\xi_e \approx 10^{-6}$ for $\mathcal{M} = 3$ shocks in a $T = 10^7 \, \mathrm{K}$, and $\xi_e \approx 6 \times 10^{-4}$ for $\mathcal{M} \geq 50$ shocks with a $T = 10^5 \, \mathrm{K}$. The additional (possible) role of shock obliquity (e.g. Wittor et al. 2017) and of fossil reaccelerated electrons (e.g. Pinzke et al. 2013) is neglected here for simplicity; we caution, however, that the additional presence of fossil electrons in cluster outskirts and in filaments will increase our estimates here, at least limited to $\mathcal{M} \leq 3-4$ shocks in the simulation (while for stronger shocks the direct injection from DSA should dominate the emission in any case). The downstream radio emission is the convolution of the several power-law distributions of electrons that overlap in the cooling region, to which we assign the integrated radio spectrum of $I(\nu) \propto \nu^{-s}$, where $s = (p - 1)/2 + 1/2$, with $p = 2(\mathcal{M}^2 + 1)/(\mathcal{M}^2 - 1)$.

An example of the radio emission at $\nu = 260 \, \mathrm{MHz}$ from our simulation is given in Fig. 2. The SKA-LOW primary beam at this frequency should be on the order of $\sim 5° \times 5°$, while our sky model covers $28.4° \times 28.4°$. The radio emission is clearly more diffuse compared to the X-ray emission, because unlike the latter it does not scale (only) with gas density, but with the shock kinetic power, which can be significant in cluster outskirts (e.g. Ryu et al. 2003). The fact that the radio power typically extends out to larger cluster radii makes it a very good probe of the rarefied cosmic web, but at the same time reduces the chances of overlap with X-ray detections, as we shall see in the next section, with a sweet spot on the scale of cluster outskirts.

3. Results

3.1. X-ray emission and radio emission from the cosmic web

We started by computing the X-ray emission from the entire simulation, as a function of environment and for different energy ranges, namely [0.3–0.8], [0.8–1.2], [1.2–2.0], [2.0–5.0], and [5.0–7.0] keV, assuming $Z = 0.3 \, Z_\odot$ everywhere. In Fig. 3 we show the median and total X-ray emission from all pixels in the sky model of Fig. 2, binned as a function of their gas temperature, which is mass-weighted along the entire line of sight[4].

At $T_{mw} \leq 5 \times 10^6 \, \mathrm{K}$ (where T_{mw} is the mass-weighted gas temperature), the X-ray emission from the WHIM is always

---

[3] https://heasarc.gsfc.nasa.gov/xanadu/xspec/manual/Models.html

[4] It is important to notice here that the average temperature values along a line of sight of 100 Mpc underestimate by a factor approximately ten (or more) the real temperature values in 3D.
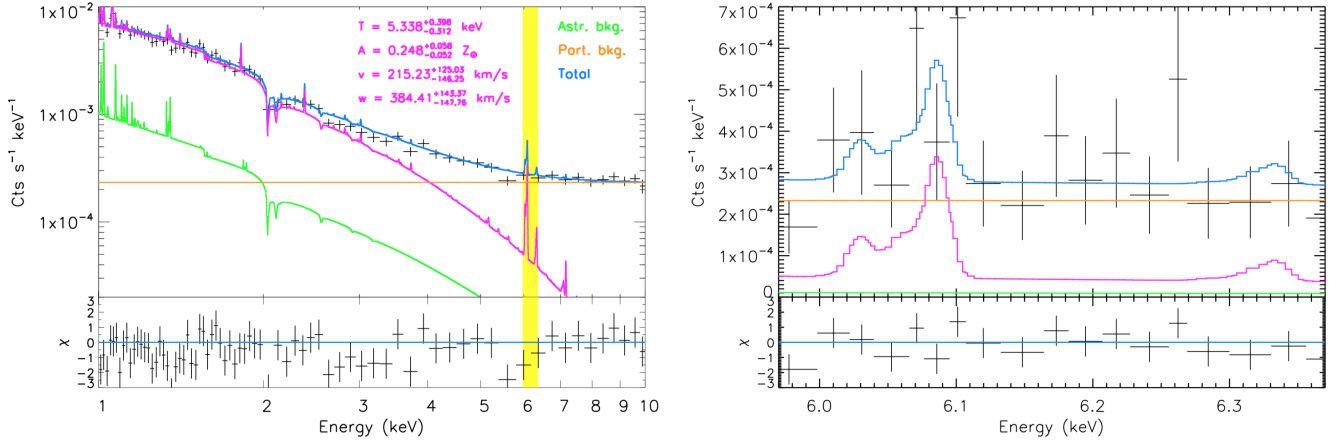
Fig. 23. SIXTE simulations of one simulated bridge in between galaxy clusters. *Left panel*: X-IFU simulated spectrum of the gas bridge and its spectral analysis. Spectral data points with error bars (black crosses) are shown with the best-fit model (blue solid line) and its three components: thermal emission from the gas (magenta), X-ray astrophysical background (green), and particle background (orange). Fit results, with errors, for the four physical quantities of the gas components are also shown. *Bottom sub-panel*: residuals with respect to the model. *Right panel*: same as *left panel*, but zooming-in on the 6–6.4 keV energy range (highlighted in yellow in the *left panel*) where the most prominent emission lines (blended Fe xxv and Fe xxvi K complexes) are present. In both panels data points have been rebinned for display purposes. The plot scaling for the spectra is logarithmic and linear in the *left and right panels*, respectively.

Table 3. Physical properties of the plasma computed in the simulation volume compared to the ones measured through the end-to-end X-IFU simulation for a 1 Ms integration with spectral fitting.

Field	Input (sim)	Output (X-IFU)
T (keV)	5.52	$5.33 \pm [-0.31, 0.40]$
v	65	$215 \pm [-146, 123]$
w	465	$384 \pm [-148, 144]$
A ($1/Z_\odot$)	0.20	$0.25 \pm [-0.05, 0.06]$

Notes. The reference (input) temperature is spectroscopic-like, v and w are the emission weighted averages, and A is the metal abundance, computed in the simulation volume as in Roncarelli et al. (2018).

statistical error of 0.3–0.4 keV and 0.05 $Z_\odot$, respectively. Most importantly, the evidence of a significant velocity dispersion is detected at high significance (more than 2.5σ), albeit with a relatively high statistical error. All the quantities are recovered with no apparent systematic bias.

However, our setup assumes a perfectly known (X-ray and particle) background. To relax this assumption, we also ran 100 Monte-Carlo spectral simulations that assumed the cluster component and propagated random fluctuations that are consistent with the current expectations on the background reproducibility in X-ray. We ran these simulations on n_H (at 1% level), on the particle background (2%), and on the remaining parameters of the background model, which are the thermal components and the power law for the unresolved cosmic X-ray background (5%). We estimate the following systematic scatter in the distribution on the best-fitting measurements of the five parameters of the bapec model: ~2%, 6%, 27%, 58%, and <1% on normalization, temperature, metal abundance, line broadening, and redshift, respectively. These results show that, while most of the parameters will be only limited by the photon counts statistic, the characterization of the emission lines in terms of total metallicity and broadening at this level of surface brightness will depend on a reliable modelling of the underlying background.

These first results offer an interesting physical application to the study of shock waves and particle acceleration in the periphery of galaxy clusters: namely a new method to constrain the shock Mach number based on spectroscopic analysis. If we assume that the measured velocity dispersion is similar to the velocity jump induced by the shock, $w \approx \Delta v' = \Delta v / \cos\phi$ (in which ϕ is the inclination of the shock normal with respect to the line of sight), and that the local sound speed is given by the temperature probed by the spectroscopy, through the "velocity-jump" method (Vazza et al. 2009) we derive

$$\mathcal{M}_{\mathrm{XIFU}} = \frac{2}{3}\left(\frac{\Delta v'}{c_s} + \sqrt{\frac{4\Delta v'}{c_s} + 9}\right), \qquad (2)$$

which yields $\mathcal{M}_{\mathrm{XIFU}} \approx 2.42$ for the X-IFU best fit values of $T \approx 5.33$ keV, $w \approx 465$ km s^{-1}, and considering $\phi \approx 75°$ for the shock normal (as suggested by Fig. 22, right panel). This is not too different from the $\mathcal{M} \sim 2.5{-}3$ range of Mach number we can measure in 3D within the X-IFU's field of view, and suggests the interesting possibility of an independent way of constraining the shock parameters via spectroscopic analysis, which can be combined and compared with the available radio information there (e.g. Mach number estimated from radio spectral indices for high resolution observations and particle acceleration efficiency). We comment that intracluster bridges, given their particular geometrical selection, may allow the performance of this study in a more robust way than in more internal regions of galaxy clusters where radio relics are found. This is because in these external regions the local sound speed is low enough and the velocity field is large enough that the Doppler broadening due to shocks with a large inclination along the line of sight may be clearly detected via spectroscopic analysis.

4. Discussion: physical and numerical uncertainties

Our results are based on non-radiative MHD simulations, in which the role of galaxy formation processes is neglected. This introduces a number of caveats due to the lack of energy losses (e.g. radiative cooling processes) and feedback processes.

In general, we expect the most relevant effects of cooling and feedback to be limited to cluster centres. Meanwhile
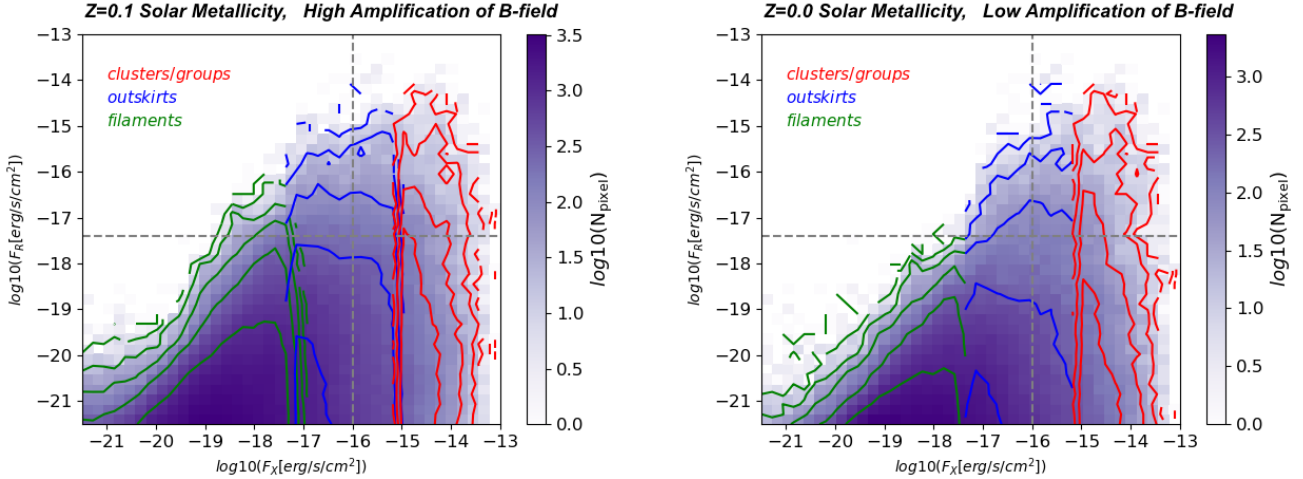
Fig. 24. Distribution of X-ray and radio flux for variations of our sky model. *Left panel*: we considered a "high amplification model" for the magnetic field and we assumed a uniform gas metallicity of $Z = 0.1\,Z_\odot$ everywhere (instead of $Z = 0.3\,Z_\odot$ as in our baseline model); in the *right panel* we considered a low-amplification model and a zero metallicity everywhere. The meaning of colours and contours is as in Fig. 5. The text gives more details on the model variations.

for $\leq 0.2R_{100}$ the combined effect of cooling, star formation, and feedback (stellar or AGN ones) can introduce a significant amount of clumping in clusters (Roncarelli et al. 2006b; Nagai & Lau 2011), as well as increase the gas density in cluster cores by approximately ten times compared to non-radiative simulations. However, such effects are predicted to be negligible at distances larger than $\sim R_{100}$ (e.g. Vazza et al. 2013), as well as within intracluster bridges.

The absence of galaxy formation processes limits our ability to model the 3D distribution of metals in the outer regions of galaxy clusters. Hence, we assume a uniform $Z = 0.3\,Z_\odot$ gas metallicity. The assumption of uniform metallicity for all elements reduces the number of free parameters making the spectral fitting presented in Sect. 3.3.4 easier. In reality, as pointed out by Cucchetti et al. (2018), the X-IFU spectral analysis will require a detailed treatment of the various emitting ions due to the chemical complexity of the ICM (see also Roncarelli et al. 2010; Biffi et al. 2013). However, most of the information on w is encoded in the Fe xxv and Fe xxvi K complexes lines (see the right panel of Fig. 23), so this simplification has a minor impact on the accuracy of our results.

In Fig. 24 we present a few variations of our model, concerning the assumed gas metallicity or the magnetic field strength in our simulation. A comparison of the two panels of Fig. 24 with Fig. 5 shows that the impact of metal line emission on the detectability of cluster outskirts is small, as the blue contours barely change. The reason for this is that in the $\sim 10^7$ K temperature range of intracluster bridges the line emission only accounts for a few percent of the total X-ray emission in the $0.8-1.2$ keV band of *Athena*-WFI.

More critical is the level of gas metallicty for any spectrosopic attempt at characterizing the local plasma condition, as in our mock X-IFU observation described in Sect. 3.3.4. However, in this case we already used the more conservative value of $0.2\,Z_\odot$ (spatially uniform everywhere) for our 1 Ms mock XIFU observation. Also in this case, a robust measurement of local plasma parameters is possible, provided that the particle and instrumental background are understood. Our tests also indicate that conversely if $Z \geq 0.1\,Z_\odot$ in intracluster bridges, the reconstruction process of gas conditions through spectroscopic analysis (even with a 1 Ms integration) will be unreliable and

dominated by large uncertainties. However, a $\sim 0.1\,Z_\odot$ metallicity is probably even too conservative, and larger metallicity values are likely present in this environment (e.g. Biffi et al. 2018; Mernier et al. 2018).

Recently, Khabibullin & Churazov (2019) reconsidered the contribution from the resonantly scattered cosmic X-ray background to the line emission for the WHIM. Resonant scattering can increase the emissivity of the WHIM considered in this work by a factor of ~ 30. However, this boost is limited to the gas at $T \leq 10^6$ K and, when integrated in the $[0.5-1]$ keV band, it is on the order of ~ 4 for the coldest part of the WHIM only. Therefore, this effect is not expected to contribute to the detectability of the much hotter gas located in intracluster bridges.

Next, we tested realistic variations of the magnetic field model, which affects the level of predicted synchrotron emission (see Fig. 24). Magnetic fields may in principle be overestimated in cosmic filaments, in case the seed fields are not of primordial origin and/or there is no dynamo amplification capable of increaseing the magnetization of the WHIM to the ~ 10 nG level (Vazza et al. 2017a). Conversely, limited to the environment of intracluster bridges, our AMR simulation can resolve the ongoing dynamo amplification of seed fields, albeit with final field strengths that are typically far from equipartition with the kinetic energy, at least in our simulation (e.g. Locatelli et al. 2018). The contribution from un-resolved gas motions by the finite numerical resolution in our scheme may underestimate the level of small-scale dynamo amplification, which becomes independent from the amplitude of seed fields for large enough Reynolds number (e.g. Cho 2014; Beresnyak & Miniati 2016). If this is the case, the $\sim 0.1-0.2\,\mu$G we measured for our intracluster bridge in Sect. 3.3.4 may be underestimated, even if to our knowledge this run is the most resolved so far for objects of this kind.

To bracket uncertainties, we followed Vazza et al. (2015b) and used a post-processing method to model two extreme scenarios for the amplification of magnetic fields in the cosmic web: a high-amplification model (HA) and a low-amplification model (LA). In both scenarios, the magnetic field strength from the simulation is renormalized a-posteriori, depending on the local gas overdensity. In the HA model, we account for the efficient magnetization of all cosmic gas denser than the critical gas mean density ($\rho \geq \langle\rho\rangle$), which cannot be resolved in the simulation.

Conversely, in the LA case we assume that the amplification can be efficient only for densities larger than that of virialized halos ($\rho \geq 300\langle\rho\rangle$). In both cases, the post-processing normalization is such that the magnetic field energy within each cell becomes equal to 1% of the cell thermal energy, if the gas density in the cell falls within the HA or LA overdensity range, or remains the original one from our baseline MHD simulation. As discussed in Vazza et al. (2015b), the two models produce very different radio fluxes, while they yield similar fluxes in the inner parts of clusters. The two panels in Fig. 24 show that the radio flux from filaments is ≥10 times larger if magnetic fields are much more amplified in filaments than our simulation can resolve. On the other hand, the predicted radio emission from cluster outskirts and from the innermost cluster regions would be only mildly increased (factors ≤4−5 on average) because, for most radio bright shocks, the magnetic energy in our simulation is not far from being ∼1% of the thermal gas energy there.

For the electron acceleration, our model only includes direct acceleration of electrons from the thermal pool (Hoeft & Brüggen 2007), but it neglects the effect of shock re-accelerated electrons (Pinzke et al. 2013; Kang et al. 2012). However, the density of fossil electrons in cluster outskirts and in bridges is largely uncertain and any level of fossil electrons will increase the emission beyond our estimates. Also, in our model we neglected for simplicity any further injection or re-acceleration of electrons by additional processes (e.g. turbulent reacceleration, re-connection, shock drift acceleration; see e.g. Brunetti & Jones 2014 and Bykov et al. 2019 for recent reviews), which, especially at low frequency, may power the emission beyond our estimates. Recent LOFAR-HBA observations suggest indeed that more volume filling and diffuse radio emission processes may be present on scales of Megaparsecs out outside of galaxy clusters. Given the above issues, the X-ray and radio emission model considered in the main paper represents a conservative lower limit on the joint detectability of intracluster bridges and extreme cluster outskirts.

5. Conclusions

We have presented mock radio and X-ray observations of the cosmic web, based on recent cosmological simulations obtained with the cosmological MHD code ENZO (Bryan et al. 2014). Extending our first exploratory study in Cassano et al. (2018), we quantified the chances of "double detecting" the shocked cosmic web in both frequency ranges, and propose best observing strategies tailored for future instruments (e.g. SKA and *Athena*). Our study highlights that the most promising targets for double detections outside of galaxy clusters are typically located in matter "bridges" connecting pairs of galaxy clusters in an earlier merger state. At this interaction stage, both radio and X-ray emission are boosted compared to the more typical conditions found in cluster outskirts. Such (transient) excess emissions appear to be within the detection range of existing (LOFAR, MWA, ASKAP) and future (SKA-LOW and SKA-MID) radio surveys, as well as of very long (≥100 ks) integrations with *Athena*, XMM, and eROSITA. Based on our simulations, the chances of double detections get greatly increased for pairs of objects with a physical (3D) association, with masses in excess of $\geq 10^{14}\,M_\odot$ and with a projected separation between one and four mean virial diameters (e.g. the sum of the two virial radii of interacting clusters). For practical purposes, a prior detection of such bridges in the radio domain is expected to serve as a strong indication of the possibility of detecting emission also in the soft (≤1.2−2 keV) X-ray band.
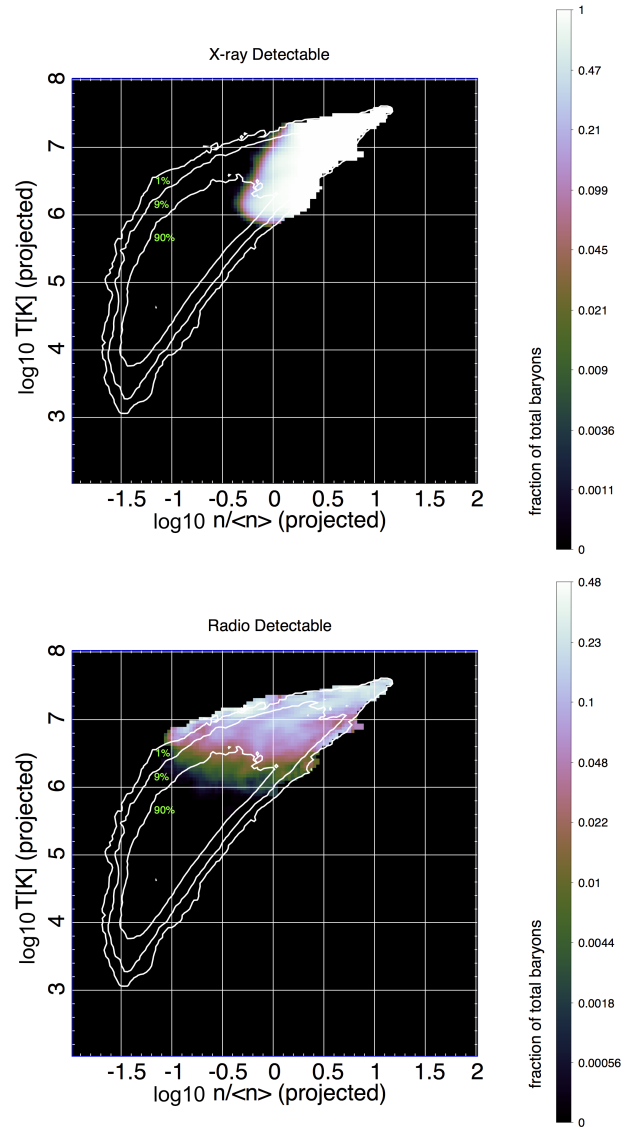

Fig. 25. Distribution of projected mean temperature and density for all pixels in our sky model at $z = 0.05$. The total area within the isocontours marks the area where the 90%, 9%, and 1% of the baryon budget is contained. The colours mark the fraction of the total baryon budget that can be detected with X-ray detections with *Athena* (*top panel*) or with radio detections with SKA-LOW (*bottom panel*).

Detecting radio emission from transient shocks in such systems will also represent a strong motivation to attempt long dedicated integrations with *Athena*'s X-IFU. For example, a deep (∼1 Ms) integration with X-IFU on such a jointly detectable portion of intracluster bridges should represent a new strong scientific case to study plasma shock physics in the rarefied environment of the WHIM. This is made possible by enabling the derivation of the shock Mach number entirely from spectroscopically-derived information of the local gas velocity dispersion and of the local sound speed, in a temperature regime that is difficult to find in galaxy clusters (Sect. 3.3.4).

Closely interacting pairs of galaxy clusters have already been detected, and observations have highlighted unexpected thermal and non-thermal gas features in the interaction region of galaxy clusters at an early merging state (e.g. Akamatsu et al. 2017; Sugawara et al. 2017; Caglar & Hudaverdi 2017; Botteon et al. 2018; Bonafede et al. 2018; Alvarez et al. 2018).

Also Sunayaev–Zeldovich observations of close pairs have hinted at the presence of dense and X-ray undetectable gas in such associations (Planck Collaboration VIII 2013; Bonjean et al. 2018).

Such objects are clearly different from cosmic filaments that are produced by simulations on much larger scales (e.g. Gheller et al. 2016). Moreover, the gas in these bridges is on a thermodynamical state that is different from the standard WHIM, as the typical density and temperature values are a factor of ∼10 larger than in the WHIM, and are more in the ICM regime. However, simulations suggest that bridges are relatively short lived (≤Gyr), and should undergo a fast evolution compared to filaments on a larger scale. They also suggest that bridges used to be part of the standard WHIM ∼1 Gyr ago, before becoming observable in the X-ray band. For this reason they have the potential of illuminating an important intermediate stage in the evolution of cosmic baryons, where gas that has been only shock-heated once in the past becomes more quickly advected onto larger clusters and is subject to large-scale mixing, reprocessing by weaker shocks, and supersonic turbulence. This leads to a transient, "boosted" WHIM phase, with a mean temperature beyond the canonical (but not entirely physically motivated) temperature bounds associated to the WHIM (10^5 K $\leq T \leq 10^7$ K).

In summary, our work stresses the importance of the radio band in studying the missing baryons of the cosmic web. We quantify this by presenting in Fig. 25 the distribution of the mean temperature and gas over density for all pixels in our sky model[11]. Contours denote the total fraction of baryons at $z = 0.05$. Overlaid is the fraction of baryons that should be detectable by X-ray observations using a 1 Ms exposure with *Athena*, or with the SKA-LOW survey at 260 MHz.

Clearly, X-ray observations are most efficient in the high-temperature and high-density part of the plot. However, less than 10% of the total budget of baryons in the Universe are located in this range. Conversely, radio surveys can trace only a much a smaller fraction of hot and dense baryons in the Universe, due to the small filling factor of shocks leading to radio emission in this regime. However, radio detections trace baryons with significantly lower projected temperature and density compared to X-ray observations, enabling them to probe into the gas phase where ∼90% of cosmic baryons are located. As such detections can only illuminate the shocked portion of the WHIM (or immediately downstream of it), it will be crucial to assess the bias factor between the radio emitting fraction of the cosmic web and its larger ("radio quiet") component. With the assistance of advanced numerical simulations capable of assessing this bias as a function of environment, wide and deep radio surveys will have the potential to convert systematic detections of radio shocks in the rarefied cosmic web into an estimate of the amount of missing baryons in the Universe.

References

Akamatsu, H., Fujita, Y., Akahori, T., et al. 2017, A&A, 606, A1
Alvarez, G. E., Randall, S. W., Bourdin, H., Jones, C., & Holley-Bockelmann, K. 2018, ApJ, 858, 44
Anders, E., & Grevesse, N. 1989, Geochim. Cosmochim. Acta, 53, 197
Arnaud, K. A. 1996, in Astronomical Data Analysis Software and Systems V, eds. G. H. Jacoby, & J. Barnes , ASP Conf. Ser., 101, 17
Bagchi, J., Enßlin, T. A., Miniati, F., et al. 2002, New Astron., 7, 249
Barcons, X., Barret, D., Decourchelle, A., et al. 2012, ArXiv e-prints [arXiv:1207.2745]
Bartels, R., Zandanel, F., & Ando, S. 2015, A&A, 582, A20
Beresnyak, A., & Miniati, F. 2016, ApJ, 817, 127
Biffi, V., Dolag, K., & Böhringer, H. 2013, MNRAS, 428, 1395
Biffi, V., Mernier, F., & Medvedev, P. 2018, Space Sci. Rev., 214, 123
Bonafede, A., Vazza, F., Brüggen, M., et al. 2013, MNRAS, 433, 3208
Bonafede, A., Brüggen, M., Rafferty, D., et al. 2018, MNRAS, 478, 2927
Bonaldi, A., & Brown, M. L. 2015, MNRAS, 447, 1973
Bonjean, V., Aghanim, N., Salomé, P., Douspis, M., & Beelen, A. 2018, A&A, 609, A49
Borm, K., Reiprich, T. H., Mohammed, I., & Lovisari, L. 2014, A&A, 567, A65
Botteon, A., Shimwell, T. W., Bonafede, A., et al. 2018, MNRAS, 478, 885
Brown, S. D. 2011, A&A, 32, 577
Brunetti, G., & Jones, T. W. 2014, Int. J. Mod. Phys. D, 23, 1430007
Bryan, G. L., Norman, M. L., O'Shea, B. W., et al. 2014, ApJS, 211, 19
Bykov, A. M., Vazza, F., Kropotina, J. A., Levenfish, K. P., & Paerels, F. B. S. 2019, Space Sci. Rev., 215, 14
Caglar, T., & Hudaverdi, M. 2017, MNRAS, 472, 2633
Cappelluti, N., Ranalli, P., Roncarelli, M., et al. 2012, MNRAS, 427, 651
Cash, W. 1979, ApJ, 228, 939
Cassano, R., Ettori, S., Giacintucci, S., et al. 2010, ApJ, 721, L82
Cassano, R., Fender, R., Ferrari, C., et al. 2018, ArXiv e-prints [arXiv:1807.09080]
Cen, R., & Chisari, N. E. 2011, ApJ, 731, 11
Cen, R., & Ostriker, J. P. 1999, ApJ, 514, 1
Cho, J. 2014, ApJ, 797, 133
Corasaniti, P. S., Ettori, S., Rasera, Y., et al. 2018, ApJ, 862, 40
Cucchetti, E., Pointecouteau, E., Peille, P., et al. 2018, A&A, 620, A173
Davé, R., Cen, R., Ostriker, J. P., et al. 2001, ApJ, 552, 473
de Graaff, A., Cai, Y.-C., Heymans, C., & Peacock, J. A. 2019, A&A, 624, A48
Dedner, A., Kemm, F., Kröner, D., et al. 2002, J. Comput. Phys., 175, 645
Domínguez-Fernández, P., Vazza, F., Brüggen, M., & Brunetti, G. 2019, MNRAS, 486, 623
Eckert, D., Molendi, S., Vazza, F., Ettori, S., & Paltani, S. 2013, A&A, 551, A22
Eckert, D., Jauzac, M., Shan, H., et al. 2015, Nature, 528, 105
Eckert, D., Ghirardini, V., Ettori, S., et al. 2019, A&A, 621, A40
Ettori, S., Ghirardini, V., Eckert, D., et al. 2019, A&A, 621, A39
Farnsworth, D., Rudnick, L., Brown, S., & Brunetti, G. 2013, ApJ, 779, 189
Gheller, C., Vazza, F., Brüggen, M., et al. 2016, MNRAS, 462, 448
Ghirardini, V., Eckert, D., Ettori, S., et al. 2019, A&A, 621, A41
Giovannini, G., Bonafede, A., Feretti, L., Govoni, F., & Murgia, M. 2010, A&A, 511, L5
Govoni, F., Orrù, E., Bonafede, A., et al. 2019, Science, 364, 981
Hickox, R. C., & Markevitch, M. 2007, ApJ, 671, 1523
Hoeft, M., & Brüggen, M. 2007, MNRAS, 375, 77
Iapichino, L., Schmidt, W., Niemeyer, J. C., & Merklein, J. 2011, MNRAS, 414, 2297
Kang, H., Ryu, D., & Jones, T. W. 2012, ApJ, 756, 97
Keshet, U., Waxman, E., & Loeb, A. 2004, ApJ, 617, 281
Khabibullin, I., & Churazov, E. 2019, MNRAS, 482, 4972
Kolodzig, A., Gilfanov, M., Hütsi, G., & Sunyaev, R. 2018, MNRAS, 473, 4653
Locatelli, N., Vazza, F., & Domínguez-Fernández, P. 2018, Galaxies, 6, 128
Loi, F., Murgia, M., Govoni, F., et al. 2019, MNRAS, 485, 5285
Lotti, S., Cea, D., Macculi, C., et al. 2014, A&A, 569, A54
Lotti, S., Mineo, T., Jacquey, C., et al. 2017, Exp. Astron., 44, 371

---

[11] As noted in Sect. 3.1, the mass-weighted temperature and volume-weighted gas density here underestimate the corresponding three-dimensional values (where most of the emission along the LOS is produced) by a factor of ∼10.

Martizzi, D., Vogelsberger, M., Artale, M. C., et al. 2019, MNRAS, 486, 3766
McCammon, D., Almy, R., Apodaca, E., et al. 2002, ApJ, 576, 188
Mernier, F., Biffi, V., Yamaguchi, H., et al. 2018, Space Sci. Rev., 214, 129
Mushotzky, R. F., Aird, J., Barger, A. J., et al. 2019, ArXiv e-prints [arXiv:1903.04083]
Nagai, D., & Lau, E. T. 2011, ApJ, 731, L10
Nevalainen, J., Tempel, E., Liivamägi, L. J., et al. 2015, A&A, 583, A142
Nicastro, F., Krongold, Y., Fields, D., et al. 2010, ApJ, 715, 854
Nicastro, F., Kaastra, J., Krongold, Y., et al. 2018, Nature, 558, 406
O'Sullivan, S. P., Machalski, J., Van Eck, C. L., et al. 2019, A&A, 622, A16
Pfrommer, C., Springel, V., Enßlin, T. A., & Jubelgas, M. 2006, MNRAS, 367, 113
Pinzke, A., Oh, S. P., & Pfrommer, C. 2013, MNRAS, 435, 1061
Piro, L., den Herder, J. W., Ohashi, T., et al. 2009, Exp. Astron., 23, 67
Planck Collaboration VIII. 2013, A&A, 550, A134
Planck Collaboration XIX. 2015, A&A, 594, A19
Planelles, S., Mimica, P., Quilis, V., & Cuesta-Martínez, C. 2018, MNRAS, 476, 4629
Roncarelli, M., Moscardini, L., Tozzi, P., et al. 2006a, MNRAS, 368, 74
Roncarelli, M., Ettori, S., Dolag, K., et al. 2006b, MNRAS, 373, 1339
Roncarelli, M., Pointecouteau, E., Giard, M., Montier, L., & Pello, R. 2010, A&A, 512, A20
Roncarelli, M., Cappelluti, N., Borgani, S., Branchini, E., & Moscardini, L. 2012, MNRAS, 424, 1012
Roncarelli, M., Gaspari, M., Ettori, S., et al. 2018, A&A, 618, A39
Ryu, D., Kang, H., Hallman, E., & Jones, T. W. 2003, ApJ, 593, 599
Schmid, C., Smith, R., & Wilms, J. 2013, SIMPUT - A File Format for Simulation Input, Tech. Report, HEASARC, Cambridge (MA)
Sheth, R., & Tormen, G. 1999, MNRAS, 308, 119
Simionescu, A., Allen, S. W., Mantz, A., et al. 2011, Science, 331, 1576
Smith, R. K., Brickhouse, N. S., Liedahl, D. A., & Raymond, J. C. 2001, ApJ, 556, L91
Sugawara, Y., Takizawa, M., Itahana, M., et al. 2017, PASJ, 69, 93
Takei, Y., Ursino, E., Branchini, E., et al. 2011, ApJ, 734, 91
Tanimura, H., Aghanim, N., Douspis, M., Beelen, A., & Bonjean, V. 2019, A&A, 625, A67
The Lynx Team 2018, ArXiv e-prints [arXiv:1809.09642]
Urban, O., Werner, N., Simionescu, A., Allen, S. W., & Böhringer, H. 2011, MNRAS, 414, 2101
Ursino, E., Galeazzi, M., & Roncarelli, M. 2010, ApJ, 721, 46
Ursino, E., Branchini, E., Galeazzi, M., et al. 2011, MNRAS, 414, 2970
Vacca, V., Murgia, M., Loi, F. G. F., et al. 2018, MNRAS, 479, 776
van Weeren, R. J., Williams, W. L., Hardcastle, M. J., et al. 2016, ApJS, 223, 2
van Weeren, R. J., de Gasperin, F., Akamatsu, H., et al. 2019, Space Sci. Rev., 215, 16
Vazza, F., Brunetti, G., & Gheller, C. 2009, MNRAS, 395, 1333
Vazza, F., Dolag, K., Ryu, D., et al. 2011, MNRAS, 418, 960
Vazza, F., Brüggen, M., & Gheller, C. 2013, MNRAS, 428, 2366
Vazza, F., Ferrari, C., Bonafede, A., et al. 2015a, ArXiv e-prints [arXiv:1501.00315]
Vazza, F., Ferrari, C., Brüggen, M., et al. 2015b, A&A, 580, A119
Vazza, F., Brüggen, M., Gheller, C., et al. 2017a, Class. Quant. Grav., 34, 234001
Vazza, F., Jones, T. W., Brüggen, M., et al. 2017b, MNRAS, 464, 210
Vazza, F., Brüggen, M., Hinz, P. M., et al. 2018a, MNRAS, 480, 3907
Vazza, F., Brunetti, G., Brüggen, M., & Bonafede, A. 2018b, MNRAS, 474, 1672
Wang, P., Abel, T., & Kaehler, R. 2010, New Astron., 15, 581
Werner, N., Finoguenov, A., Kaastra, J. S., et al. 2008, A&A, 482, L29
Wittor, D., Vazza, F., & Brüggen, M. 2017, MNRAS, 464, 4448
Zhuravleva, I. V., Churazov, E. M., Sazonov, S. Y., Sunyaev, R. A., & Dolag, K. 2011, Astron. Lett., 37, 141